

Saltating Characteristics of Particle Motions Near the Channel Bed

HONG-YUAN LEE*** AND IN-SONG HSU**

**Department of Civil Engineering
National Taiwan University
Taipei, Taiwan, R.O.C.*

***Hydraulic Research Laboratory
National Taiwan University
Taipei, Taiwan, R.O.C.*

(Received May 8, 1997; Accepted November 24, 1997)

ABSTRACT

A real-time flow visualization technique and a high-speed photographic technique were developed in this study to measure particle trajectories, velocities, and spinning rates. Different combinations of water depths, channel slopes, particle sizes, particle shapes, and particle densities were tested. Regression equations for the dimensionless average saltation length, height, and velocity, lift-off spinning rates and longitudinal variations of the spinning rates were obtained. A mathematical model which is able to simulate particle single-step saltation behaviors is developed herein. This model is able to calculate the particle trajectories and the longitudinal variations of the velocities, accelerations, and corresponding forces acting upon the particle. The simulated saltation trajectories agree well with the experimental data. It is also found that the Saffman force and Magnus force play a very important role in the saltation process and, hence, cannot be neglected.

Key Words: sediment transport, bed load transport, saltation, real-time flow visualization technique, high-speed photographic technique

I. Introduction

Transport of sediment particles in water can be classified into three different modes, namely, rolling or sliding, saltation, and suspended motion. The type of transport depends on the size and location of the bed materials and the flow conditions. A particle begins to move, by sliding or rolling over the bed, when the bed shear stress exceeds the critical value for initiation of motion. But with a small increase in the bed shear stress, these particles hop up from the bed and follow ballistic trajectories. This mode of transport is known as saltation. The transport of particles by rolling, sliding, and saltating is called bed load transport. Saltation is the dominant mode of bed load transport, with rolling and sliding occurring to a lesser extent. Hence, investigation of particle saltating motions is crucial to the development of bed load transport theories.

The saltation behaviors have been studied by a number of researchers. Based on his flume study, Einstein (1950) found the thickness of the bed load to be about two times the particle size and the saltation

length to be about 100 times the particle size. The saltation length was found to be a function of particle size, shape, and hydraulic characteristics. Fernandez Luque and Van Beek (1976), Abbott and Francis (1977), and Murphy and Hooshiari (1982) investigated saltation in water using high-speed photography and determined the saltation height and length as well as average particle velocity. Van Rijn (1984) used the particle saltation characteristics to derive a bed-load transport formula. Wiberg and Smith (1985) proposed a mathematical model that described the trajectory of a saltating particle as a function of time. Using a stochastic method, Sekine and Kikkawa (1992) proposed a model to describe sequent saltating motions.

Due to the combined effects of bed roughness and velocity gradient, particles spin during the saltating process. The spinning motion generates an additional lift force, known as the Magnus force, and thus increases the saltation length and height. The increments can be as high as 12% (Lee and Hsu, 1994). Because of experimental difficulties, Magnus effects of particle saltation were generally assumed to be negligible in previous saltation models (Fernandez Luque and Van

Beek, 1976; Abbott and Francis, 1977; Murphy, 1982; Van Rijn, 1984). Observing bright and dark spots in the photographs of saltating particles, Chepil (1945) roughly estimated that the spinning rate of the saltating particles in air was between 200 to 1,000 revolutions/sec. Using a high-speed camera, White and Schultz (1977) found the particle spinning rate to be between 100 and 300 revolutions/sec in air. Hui and Hu (1991) conducted flume experiments and found the particle spinning rate to be about 40 revolutions/sec in water.

Two different measuring techniques were developed in this study to measure the kinematic characteristics of saltating motions. A real-time flow visualization technique was applied to investigate particle saltations near the channel bed. With this technique, particle trajectories and average velocities were measured without disturbing the flow field. A high-speed photographic technique was also applied in this study to measure the saltating trajectories and corresponding spinning rates. The longitudinal variations of the saltation velocities and the spinning rates under varied flow conditions were recorded. Regression equations for the dimensionless saltation length, height, average velocity, lift-off spinning rates and longitudinal variations of the spinning rates were obtained. A mathematical model for single-grain saltation is also proposed. The gravity force, added-mass force, drag force, lift force, Saffman force, and Magnus force are included. The model has been calibrated and verified with the experimental data, and the results have been found to be quite satisfactory.

II. Theoretical Analysis

The parameters that affect the characteristics of saltation can be classified into three categories, namely, hydraulic conditions, particle characteristics and bed configurations. The characteristics of saltation can be expressed as a function of the independent variables as

$$Y_S = f_1(U_*, \rho_w, \mu, D, \rho_s, d, g), \quad (1)$$

in which Y_S = hydraulic characteristic of saltation; U_* = shear velocity, $U_* = \sqrt{gHS_o}$, H = flow depth, S_o = bed slope; ρ_w and μ = density and dynamic viscosity of water, respectively; D and ρ_s = diameter and density of the saltating particle, respectively; d = size of bed materials and g = gravitational acceleration. Using Buckingham's II method, Lee and Hsu (1994, 1996) suggested the following functional relationship:

$$\bar{Y}_S = f_2(D^*, T^*, D_r), \quad (2)$$

in which \bar{Y}_S = hydraulic dimensionless characteristic of saltation, including $D_r = \frac{d}{D}$, $D^* = D \left[\frac{(S-1)g}{v^2} \right]^{\frac{1}{3}}$ and $T^* = \left[\frac{(U_*)^2 - (U_{*c})^2}{(U_{*c})^2} \right]$, U_{*c} = critical shear velocity, $S = \frac{\rho_s}{\rho}$ and v = kinematic viscosity of water.

III. Experimental Setup

1. Real-time Flow Visualization Technique

The experiments were conducted in a 12-m-long, 0.3-m-wide slope-adjustable recirculating flume. Several combinations of water depth, channel slope, and particle size were tested. The range of water depth was from 3.71 cm to 12.08 cm, and the range of the slope was from 0.0002 to 0.023. The range of the shear velocity U_* was from 0.036 m/s to 0.105 m/s. The range of the Froude number was from 0.569 to 2.023. Uniform sand of size 1.36 mm was glued to the channel bed to form a rough surface. The effective roughness of the bed surface was about 1.36 mm. Two particle sizes, with mean diameters equal to 1.36 mm and 2.47 mm, were used. The specific gravity was 2.64. The flow was turbulent. The Reynolds number was between 21,000 and 73,000, and the roughness Reynolds number varied between 50 and 146. For details of the experimental arrangements, please refer to Lee and Hsu (1994).

To measure the instantaneous particle saltation trajectories accurately and efficiently, a real-time flow visualization technique was used. The general configuration of the experimental setup is shown in Fig. 1. The light source was generated by a 4-W argon ion laser. It passed a beam steering device and three mirrors to reach the top of the flume. Another beam steering device and a cylindrical mirror were applied to create a light sheet passing through the center plane of the flume. The thickness of the light sheet was adjustable and was between 1 mm and 2 mm. The light sheet had to be longer than the working section, which was between 5 cm and 15 cm. In the experiment, sediment particles were released about 2 m upstream of the working section. As the saltating particles passed through the light sheet, laser light was reflected and recorded by a charge couple device camera (CCD camera).

The image obtained from the CCD camera was first processed and stored by an image-processing board installed in an IBM PC 486-50 computer. The image stored was then digitized using an input lookup table (ILUT). Different gray levels were assigned to images collected at different times. The digitized images were then processed by an arithmetic-logic unit (ALU) and

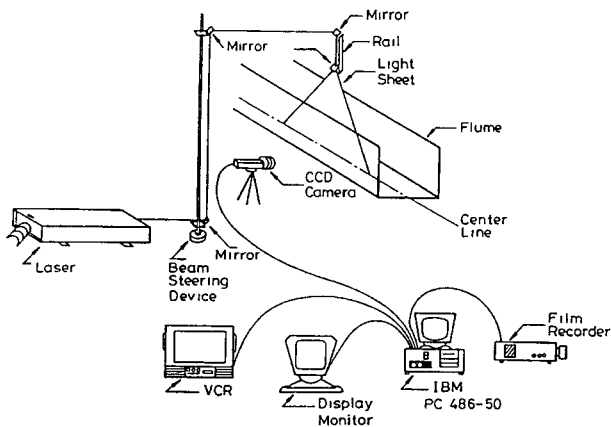


Fig. 1. Experimental setup (1).

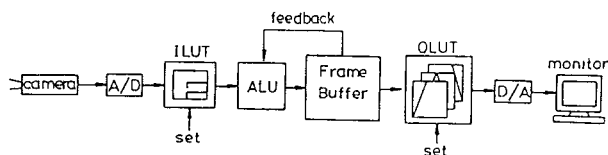


Fig. 2. Image-processing system.

stored in a frame buffer zone. After several hundred images were accumulated, the images were processed using an output lookup table (OLUT). Different colors were assigned to different gray levels. The final colored particle trajectory was thus obtained and shown on the display monitor. Each color represented a different time interval, and the length of the color segment represented the distance traveled during the time interval. The instantaneous velocity vector could thus be obtained. In the present experiment, the time interval chosen was 1/30 sec; that is, 30 pictures were taken in 1 sec, and seven different colors (red, orange, blue, pink, yellow, navy blue, and gray) were assigned to represent different time intervals. The flowchart of the image-processing system is shown in Fig. 2, and a typical particle trajectory is shown in Fig. 3. In Fig. 3, the particle is saltating from right to left. Totally, there are five colored segments in this picture: orange, blue, pink, yellow, and navy blue. The time interval of each color is 1/30 sec; hence, the total time span for this trajectory is 1/6 sec.

2. High Photographic Technique

The experiments were conducted in a 12-m-long, 0.3-m-wide slope-adjustable recirculating flume. Several combinations of water depth, channel slope, and particle type were tested. The range of water depth was from 4.6 cm to 7.8 cm, the range of the slope was

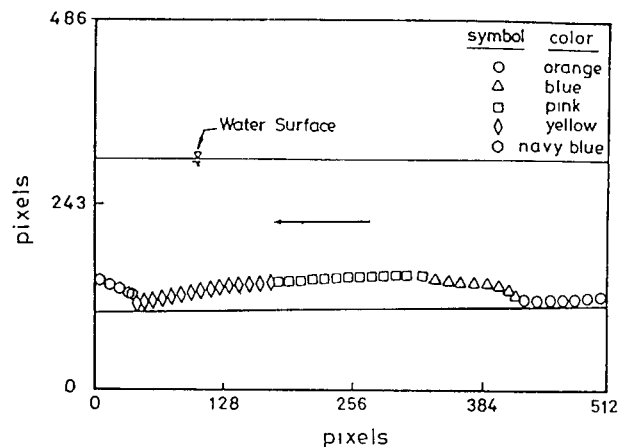


Fig. 3. Saltation trajectory (1).

from 0.0031 to 0.0198, and the range of the shear velocity U_* was from 0.04 m/sec to 0.102 m/sec. The range of the flow velocity was from 0.554 m/s to 1.173 m/s. The range of the Froude number was 0.677 to 1.530. Plastic balls of diameter 5.95 mm were glued to the channel bed to form the bed surface. The Reynolds number was between 26,100 and 53,500. Five particles of various sizes, shapes and specific gravities were used in the experiments. The particles were marked with crosses in blue and red lines, and the spinning rates were determined according to the rotating angles of the crosses. For details of the experimental arrangements, please refer to Lee and Hsu (1996).

A strobo light located at the top of the flume was used as the light source. The maximum frequency of the strobo light was 3,000 flash/sec. Two 35 mm conventional cameras loaded with 400 ASA films were used to take photographs. The general configuration of the experimental setup is shown in Fig. 4. During the experimental process, the room was kept in complete darkness, and the only light source was from the strobo. The camera shutter and the strobo were set to be synchronous, so that the intervals between the particles shown on the photograph were constant. The frequency of photographs taken depended on the flow conditions and the particle-saltating velocities. A low frequency resulted in a large distance between the particle images and, thus, diminished the accuracy of the experiments. If the frequency was too high, the images overlapped, making the photographs useless. By trial and error, the frequency of the strobo was set to be 50 Hz. During the experimental process, the marked particles were released 4 m from the working section, and the saltating trajectories were recorded by the camera. The photographs were then projected onto a big screen to measure the saltating velocities and the

Saltating Characteristics of Particle Motions

Table 1. The Real-time Flow Visualization Experiments

Run	Slope	Average Velocities	Froude number	Transport stage parameter T_*	Average saltation length \overline{L}_s/D	Average saltation height \overline{H}_s/D	Average longitudinal saltation velocity \overline{U}_s/U_*
R1	0.002	0.619	0.569	1.308	14.5	2.3	6.4
R2	0.006	0.689	1.143	2.077	20.0	2.6	6.9
R3	0.006	0.644	0.926	2.846	24.6	3.1	7.5
R4	0.016	1.125	1.668	3.516	32.4	3.8	7.7
R5	0.016	1.386	1.730	4.806	40.0	4.7	8.1
R6	0.016	1.415	1.635	5.452	48.2	5.1	8.4
R7	0.016	1.103	1.654	8.615	59.1	5.9	9.1
R8	0.016	1.264	1.677	10.538	69.0	6.7	9.4
R9	0.016	1.426	1.694	12.462	85.3	7.4	9.6
R10	0.020	1.485	1.882	14.385	93.2	8.2	9.7
R11	0.023	1.495	1.926	16.308	101.0	9.0	9.8
R12	0.023	1.595	2.023	16.692	105.0	9.2	9.9

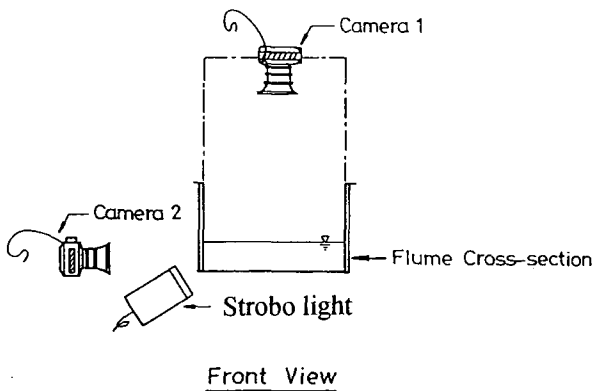


Fig. 4. Experimental setup (2).



Fig. 5. Saltation trajectory (2).

corresponding spinning rates. A typical trajectory of the spinning motions during the saltation process is shown in Fig. 5.

IV. Experimental Results

1. Average Saltation Length, Height, and Velocity

Important results of the real-time flow visualization experiments are summarized in Table 1, where

$$T_* = \frac{(U_*)^2 - (U_{*c})^2}{(U_{*c})^2} \text{ and } D_* = D \left[\frac{(S-1)g}{\nu^2} \right]^{\frac{1}{3}}$$

are the transport stage parameter and particle parameter, respectively. \overline{L}_s , \overline{H}_s , and \overline{U}_s are the average saltation length, height, and longitudinal velocity, respectively. The range of the transport stage parameter was between 1.308 and 16.692. The range of the dimensionless average saltation length \overline{L}_s/D was from 14.5 to 105; that of the dimensionless saltation height \overline{H}_s/D was

from 2.2 to 9.2; and that of the dimensionless average longitudinal saltation velocity \overline{U}_s/U_* was from 6.4 to 9.9. The average saltation length, height, and velocity were found to increase as the transport stage parameter increase.

The average longitudinal particle velocity was slow in the rising limb of the trajectory, reached a maximum value in the central portion, and then slowed down in the falling limb. This can be explained as follows. In the rising limb, the sediment particle was picked up by water and transported to a higher velocity zone. Hence, it was accelerating. Up to a certain elevation, the relative velocity decreased; thus, the Saffman force and Magnus force decreased accordingly. The particle started to settle down due to gravity and thus decelerated. Also due to the inertia effect, the velocity in the falling limb was larger than the velocity in the rising limb. This feature can be simulated in the mathematical model developed in the study.

Regression equations for the dimensionless average saltation length, height, and velocity were obtained

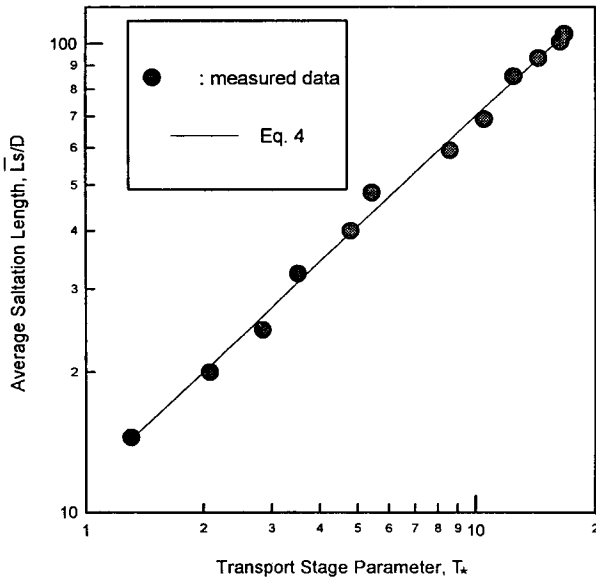


Fig. 6. Simulated and measured dimensionless average saltation length.

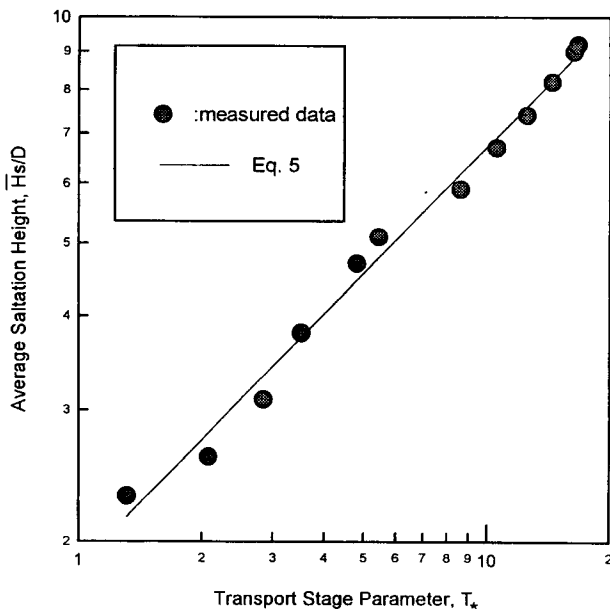


Fig. 7. Simulated and measured dimensionless average saltation height.

and are listed as follows:

$$\log\left[\frac{\bar{L}_s}{D}\right] = 0.778 \log[T_*] + 2.455 \quad (3)$$

$$\log\left[\frac{\bar{H}_s}{D}\right] = 0.558 \log[T_*] + 0.618 \quad (4)$$

$$\log\left[\frac{\bar{U}_s}{D}\right] = 0.172 \log[T_*] + 1.822. \quad (5)$$

The R^2 values of Eqs. (3), (4), and (5) are 0.995, 0.990, and 0.992, respectively. The predicted and estimated values are shown in Figs. 6-8. The results are satisfactory. The applicable range of these equations is $T_* = 1.308$ -16.692. These results are similar to those of Lee and Hsu (1994).

2. Spinning Motion during Saltating Process

According to the experimental observations, particle spinning is a combined effect of its collision with the bed, the velocity gradient, and the particle shape. The axes of the spinning motion can be: parallel to the channel bed and perpendicular to the flow direction; parallel to the channel bed and in the flow direction; or perpendicular to the channel bed. These motions are known as top-spin, screw-spin, and side-spin motions, respectively. Under uniform flow conditions, the saltating processes are dominated by top-spin motion. Side-spin and screw-spin motions exist only at an early stage of the rising limb of the process.

The experimental results are summarized in Table 2. The transport stage parameter T_* ranged from 0.37 to 27.53, and the particle parameter D_* varied from 57.1 to 171.8. The average lift-off spinning rate was between 11.24 and 31.8 revolutions/sec. Table 2 indicates that the spinning rate increased as the transport

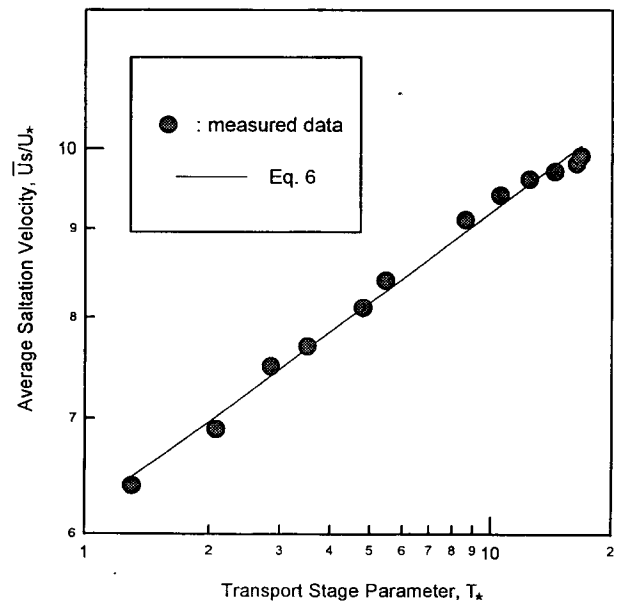


Fig. 8. Simulated and measured dimensionless average saltation velocity.

Saltating Characteristics of Particle Motions

Table 2. The High Photographic Technique Experiments

Run	Slope	Average Velocities	Froude number	Transport stage parameter T_*	Saltating to bed particle size ratio D_r	Particle parameter D_*	Average lift-off spin-rate $\bar{\omega}_L$	Average lift-off spinning parameter $\bar{\Omega}_L$
1	0.0031	0.554	0.705	12.23	1.0	57.1	11.24	14.45
2	0.0031	0.673	0.729	16.11	1.0	57.1	12.49	13.50
3	0.0052	0.601	0.797	20.78	1.0	57.1	14.35	13.27
4	0.0052	0.750	0.858	27.53	1.0	57.1	16.20	12.66
5	0.0052	0.592	0.785	0.37	1.0	163.9	18.29	92.30
6	0.0052	0.592	0.677	0.79	1.0	163.9	20.34	51.30
7	0.0083	0.780	1.018	1.22	1.0	163.9	21.73	37.70
8	0.0115	0.859	1.176	1.81	1.0	163.9	24.30	30.50
9	0.0136	0.900	1.286	2.20	1.0	163.9	25.12	27.10
10	0.0157	0.934	1.334	2.58	1.0	163.9	27.10	25.80
11	0.0178	0.973	1.419	2.91	1.0	163.9	27.70	24.05
12	0.0198	1.015	1.512	3.20	1.0	163.9	27.86	22.52
13	0.0198	1.173	1.530	4.35	1.0	163.9	31.83	20.57
14	0.0083	0.780	1.017	1.32	1.1	171.8	21.19	38.54
15	0.0115	0.859	1.176	1.95	1.1	171.8	23.48	31.27
16	0.0136	0.900	1.286	2.35	1.1	171.8	24.28	27.91
17	0.0157	0.934	1.334	2.75	1.1	171.8	25.43	25.92
18	0.0178	0.973	1.419	3.10	1.1	171.8	26.98	25.14
19	0.0198	1.015	1.512	3.41	1.1	171.8	27.56	23.96
20	0.1098	1.173	1.530	4.61	1.1	171.8	29.73	20.74
21	0.0083	0.780	1.017	2.36	0.8	125.0	18.32	24.87
22	0.0115	0.859	1.176	3.23	0.8	125.0	20.42	16.10
23	0.0136	0.900	1.286	3.80	0.8	125.0	22.09	15.42
24	0.0157	0.934	1.334	4.38	0.8	125.0	22.86	14.43
25	0.0178	0.973	1.419	4.88	0.8	125.0	23.42	13.69
26	0.0198	1.015	1.512	5.31	0.8	125.0	24.94	13.73
27	0.0198	1.173	1.530	7.04	0.8	125.0	26.50	12.01
28	0.0052	0.724	0.828	2.65	0.7	102.5	17.57	15.72
29	0.0083	0.780	1.017	3.53	0.7	102.5	19.44	14.05
30	0.0115	0.859	1.176	4.75	0.7	102.5	21.05	12.29
31	0.0136	0.900	1.286	5.54	0.7	102.5	22.68	11.89
32	0.0157	0.934	1.334	6.31	0.7	102.5	23.14	11.08
33	0.0178	0.973	1.419	6.99	0.7	102.5	25.46	11.37
34	0.0198	1.015	1.512	7.59	0.7	102.5	26.52	11.21
35	0.0198	1.173	1.530	9.94	0.7	102.5	28.37	10.03

stage parameter T_* , the specific gravity of the saltating particle, and the relative size of the saltating particle D_r increased. Under the same flow conditions and similar specific gravity of the saltating particles, the average lift-off spinning rate of a spherical particle was slightly larger than that of a natural sand.

As shown in Fig. 9, the spinning rate decreased linearly along the trajectory. Also, as shown in Fig. 9, a spherical particle spun more rapidly than did a natural sand, and the result of the natural sands was more irregular than that of the spherical particles. To investigate the influence of T_* , D_* , and D_r on the dimensionless average lift-off spinning rate, the experimental results of various particle sizes, shapes, and specific gravities were analyzed and are shown in Fig. 10. This figure indicates that $\bar{\Omega}_L$ decreased as T_* increased. $\bar{\Omega}_L$ can be expressed as $\bar{\omega}_L \cdot D / (U_* - U_{*c})$,

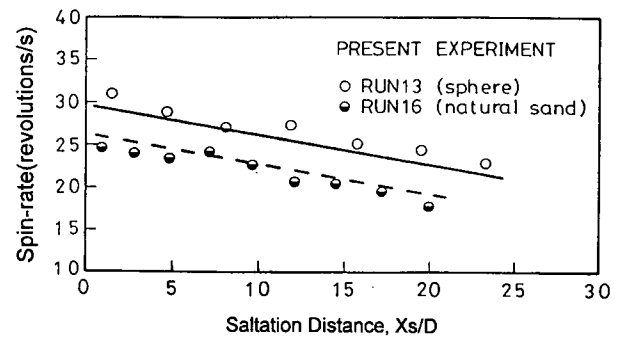


Fig. 9. The longitudinal variations of the saltation spinning rate.

where $\bar{\omega}_L$ =average lift-off spinning rate, U_* =flow shear velocity, and U_{*c} =critical shear velocity of the particle. According to Table 2, a larger $\bar{\omega}_L$ resulted in a smaller $\bar{\Omega}_L$; hence, we can conclude that the particle spun more

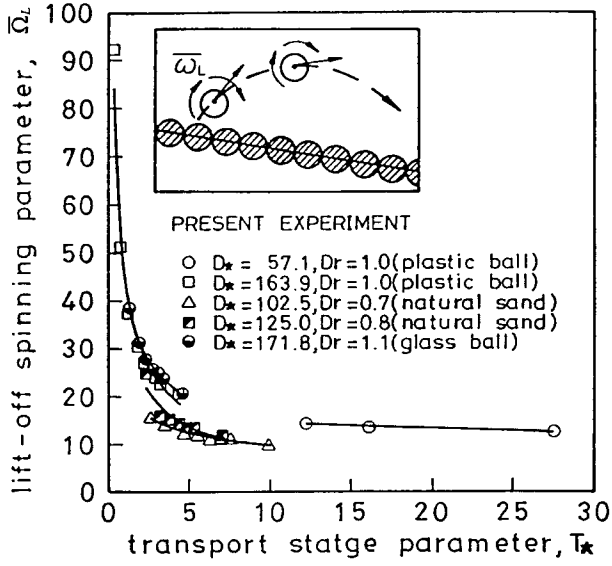


Fig. 10. The variations of the lift-off spinning rate.

rapidly as the sediment transport capacity increased. Under the same T_* , particles with larger sizes and specific gravity spun more rapidly. The reason is that larger and heavier particles tended to generate larger reactive forces when they collided with the channel bed. Hence, particles with sizes smaller than the bed materials spun more slowly, and particles the same size as the bed materials spun more rapidly. Leaving data of runs 13 and 16 for verification, a regression equation for the dimensionless average lift-off spinning rate is

$$\bar{\Omega}_L = 348.24(T_*)^{-0.55}(D_*)^{-0.41}(D_r)^{1.41}. \quad (6)$$

The R^2 values=0.94, and the applicable range of this equation is $T_*=0.37-27.53$, $D_*=57.1-171.8$, and $D_r=0.7-1.1$. Similarly, leaving data of runs 13 and 16 for verification, a regression equation for the longitudinal variation of the spinning rate can be obtained:

$$\bar{\omega}_s = \bar{\omega}_L + a(X_S/D), \quad (7)$$

where $\bar{\omega}_s$ =average spinning rate; X_S =longitudinal salutation distance; and a =a constant between -0.30 and -0.44. To simplify calculation, an average value of -0.35 was set. The R^2 values=0.88. The applicable range of this equation is the same as that of Eq. (7). These results are similar to those of Lee and Hsu (1996).

Knowing the hydraulic characteristics and properties of the saltating particles, the spinning rate along the trajectory can be computed using Eqs. (7) and (8). The observed and predicted values of runs 13 and 16 are shown in Fig. 9. The accuracy is quite satisfactory.

V. Mathematical Model

1. Model Formulation

The forces acting on saltating particles include the submerged weight, drag force, added-mass force, lift force, Saffman force, and Magnus force. The Basset history term, associated with the growth and decay of the boundary layer on particles as the relative velocity changes, is assumed to be negligible (Wood and Jenkins, 1973). The forces are discussed in the following.

(1) Submerged Weight (E_G)

The submerged weight is expressed as:

$$E_G = \alpha_V(\rho_s - \rho_w) g D^3, \quad (8)$$

where α_V =volume coefficient, which equals $1/6\pi$ for a sphere, and ρ_w and ρ_s =densities of water and particle, respectively.

(2) Drag Force (E_D)

The drag force is caused by a combination of the pressure difference and skin friction and is expressed as:

$$E_D = C_D \alpha_A \frac{D^2}{2} (\underline{V} - \underline{V}_S) \cdot |\underline{V} - \underline{V}_S|, \quad (9)$$

where C_D =drag coefficient, and $\alpha_A D^2$ =projected area perpendicular to the flow direction; α_A is the area coefficient; and \underline{V} and \underline{V}_S =velocities of the flow and particle. The drag coefficients were evaluated using the empirical relation of Morsi and Alexander (1972).

(3) Added Mass Force (E_A)

The added mass force depends on the relative acceleration of a body with respect to the surrounding fluid, resulting in an apparent mass in addition to the real mass of the body. This force is proportional to the mass of the displaced fluid times the relative acceleration:

$$E_A = -\alpha_M \rho_w \alpha_V D^3 \left(\frac{d\underline{V}}{dt} - \frac{d\underline{V}_S}{dt} \right), \quad (10)$$

where $\left(\frac{d\underline{V}}{dt} - \frac{d\underline{V}_S}{dt} \right)$ is the relative acceleration, and α_M is the added mass coefficient. For a sphere, $\alpha_M=0.5$, and for most sediment grains, α_M is close to 0.5.

(4) Lift Force (E_L)

Several different formulas are available for calculating the lift force. Fluid-dynamic lift is caused by the flow shear stress and the irregular shape of the saltating particle. The former, which is regarded as the Saffman force (Saffman, 1965),

gives rise to a pressure gradient normal to the shear in the direction of increasing velocity. The latter is be regarded as the general lift force in this paper. The lift force due to the irregular shape is expressed as:

$$F_L = C_{L1} \alpha_A \rho_w \frac{D^2}{2} (\underline{V} - \underline{V}_s) \cdot |\underline{V} - \underline{V}_s|, \quad (11)$$

where C_{L1} =lift coefficient. It equals zero for a sphere.

(5) Saffman Force (F_S)

Saffman's equation (Saffman, 1965) can be written as:

$$F_S = C_{L2} \rho_w \nu^{0.5} D^2 (\underline{V} - \underline{V}_s) \cdot |\underline{V} - \underline{V}_s| \left(\frac{\partial \underline{V}}{\partial z} \right)^{0.5}, \quad (12)$$

where $\frac{\partial \underline{V}}{\partial z}$ =velocity gradient, and C_{L2} =Saffman lift coefficient. The Saffman lift coefficient is a function of the Reynolds number $R_* = U_* D / \nu$; $C_{L2} = 1.6$ when $R_* \leq 5$, $C_{L2} = 20$ when $R_* \geq 70$, and it varies linearly from 1.6 at $R_* = 5$ to 20 at $R_* = 70$.

(6) Magnus Force (F_M)

The lift force due to the Magnus effect was calculated using Rubinow and Kellers' formula (Rubinow and Keller, 1961):

$$F_M = C_{L3} \rho_w D^3 \underline{V}_r \times \underline{V}_\omega, \quad (13)$$

where $\underline{V}_\omega = 2\pi \underline{\omega}_s$ is the particle angular velocity, $\underline{\omega}_s$ =saltation spinning rate; C_{L3} =Magnus lift coefficient, which equals 0.4 for the viscous flow; and \underline{V}_r is the relative velocity.

Substituting the above mentioned force components into the equation of motion, the governing equation is obtained. This equation is similar to those of White and Schultz (1977), Van Rijn (1984), Wiberg and Smith (1985), and Lee and Hsu (1994):

$$\begin{aligned} m_s \frac{d \underline{V}_s}{dt} = & \alpha_v (\rho_s - \rho_w) D^3 \underline{g} + C_D \alpha_A \rho_w \frac{D^2}{2} (\underline{V} - \underline{V}_s) \\ & \cdot |\underline{V} - \underline{V}_s| - \frac{1}{2} \rho_w \alpha_v D^3 \left(\frac{d \underline{V}}{dt} - \frac{d \underline{V}_s}{dt} \right) \\ & + C_{L2} \sqrt{\rho_w \mu} (\underline{V} - \underline{V}_s) \cdot |\underline{V} - \underline{V}_s| \cdot \sqrt{\frac{\partial \underline{V}}{\partial z}} \\ & + C_{L3} \rho_w D^2 \underline{V}_r \times \underline{V}_\omega, \end{aligned} \quad (14)$$

where m_s =the mass of sediment grain; $\underline{V}_s = U_s \underline{i} + W_s \underline{j}$ is the instantaneous velocity of the saltating particle; U_s and W_s =longitudinal and vertical components of the particle velocity; $\underline{V} = U(z) \underline{i}$ is the flow velocity; and

$\underline{V}_r = [(U - U_s)^2 + (W_s)^2]^{0.5}$. The above mentioned equation can be further simplified as

$$\begin{aligned} m_s \frac{d \underline{V}_s}{dt} + F_A \left(\frac{U - U_s}{V_r} \right) - (F_S + F_M) \left(\frac{W_s}{V_r} \right) \\ - F_D \left(\frac{U - U_s}{V_r} \right) - F_G \sin \varphi = 0 \end{aligned} \quad (15)$$

$$\begin{aligned} m_s \frac{d \underline{W}_s}{dt} + F_A \left(\frac{W_s}{V_r} \right) - (F_S + F_M) \left(\frac{U - U_s}{V_r} \right) \\ - F_D \left(\frac{W_s}{V_r} \right) - F_G \cos \varphi = 0, \end{aligned} \quad (16)$$

where φ =channel bed slope.

2. Flow Condition

The vertical-flow distribution is affected by the roughness Reynolds number $R_* = U_* K_s / \nu$, where K_s =equivalent roughness height. The velocity distribution is described by the logarithmic law

$$U(z) = \frac{U_*}{\kappa} \ln(z / z_o), \quad (17)$$

where $\kappa=0.4$ is the Karman constant; $z_o=0.11(\nu / U_*) + 0.033 K_s$ is the elevation where velocity equals zero.

3. Boundary Condition

The initial position of the particle was assumed to be $0.50 D$ from the channel bed. According to Abbott and Francis (1977), the average longitudinal and vertical components of the lift-off velocity are approximately equal to $2U_*$.

4. Numerical Technique

The governing equations, Eqs. (15) and (16), are second-order nonlinear partial differential equations. They were transformed into a system of first-order differential equations and then solved using the fourth-order Runge-Kutta method.

VI. Results and Comments

1. Calibration and Simulated Results

The calibration procedure and results are similar to those of Lee and Hsu (1994) and, hence, will not be discussed in detail herein. Using the relations of Eqs. (6) and (7), the variations of the spin-rates under the saltating process can be determined. Substituting

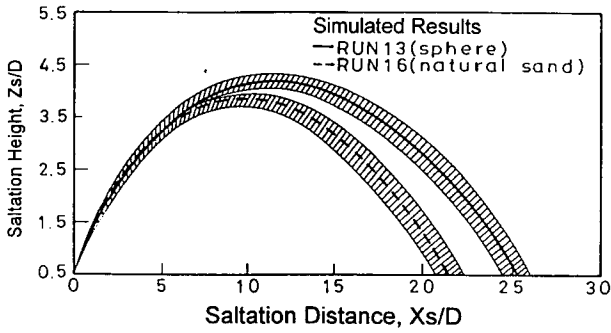


Fig. 11. The simulated results of the saltation trajectories.

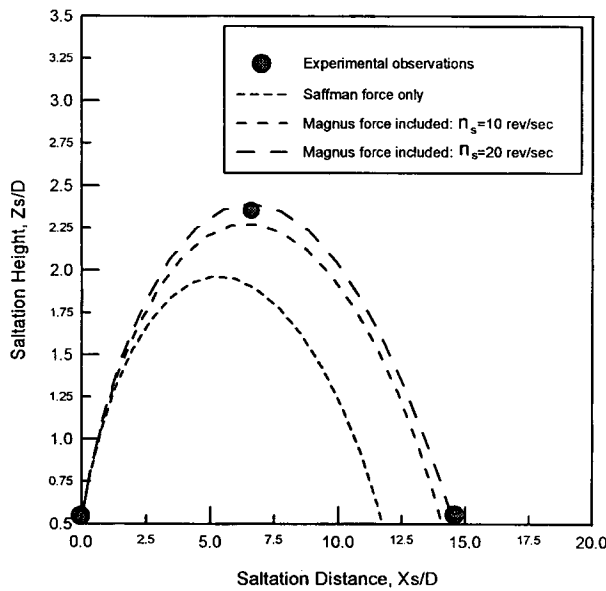


Fig. 12. Influence of the Magnus effect on the characteristics of particle saltation.

these data into the mathematical model, the saltating trajectories and the corresponding kinematic characteristics can be determined. The simulated saltating trajectories are shown in Fig. 11. It shows that the measured and simulated particle trajectories are very close for various combinations of flow and sediment conditions.

2. Influence of Magnus Effect

White and Schultz (1977) conducted a series of wind tunnel experiments and obtained a particle spinning rate of 100-300 revolutions/sec in wind sediment transport. Hui and Hu (1991) conducted a series of flume tests and obtained a spinning rate of about 40 revolutions/sec in water sediment transport. Regression equations for the dimensionless averaged lift-off spinning rates and longitudinal variations of the spin-

ning rates were obtained in this study. Rubinow and Kellers' relation (Rubinow and Keller, 1961), i.e., Eq. (13), was applied in the mathematical model to investigate the influence of the Magnus effect on the characteristics of the particle saltation. The results are shown in Fig. 12. It shows that the saltation length and height increase significantly as the spin rate increases. The simulation result with a spin rate of 20 revolutions/sec agrees well with the experimental data. Comparing this result with the case without spinning motion, it is found that the saltation length and height increase 28% and 20%, respectively. These increments are larger than the number suggested by Lee and Hsu (1994).

3. Influence of Lift-Off Velocities and Angles

The lift-off velocities and angles are associated with rebounding of the saltating particles from the channel bed. They depend on the channel-bed configurations and the approaching angles, and hence are random processes. Four different combinations of the velocity components and angles were simulated. The results are shown in Fig. 13. It shows that the saltation length and height increase as the lift-off angle increase. The particle with a larger vertical lift-off velocity component tends to have larger saltation height and length. This is due to the particle's acquisition of momentum during the saltation process. The particle with a larger vertical lift-off velocity component is transported to a higher elevation and gains more momentum there; thus, the saltation height and length

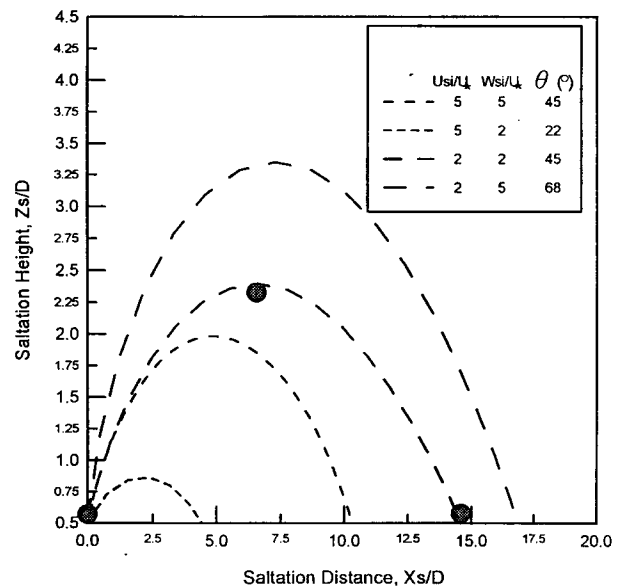


Fig. 13. Influence of the lift-off velocities and angles on the saltation trajectories.

increase.

4. Spatial Variations of Saltation Characteristics

The spatial variations of the particle velocities for various flow conditions were simulated and the results are shown in Figs. 14 and 15. The particle accelerates

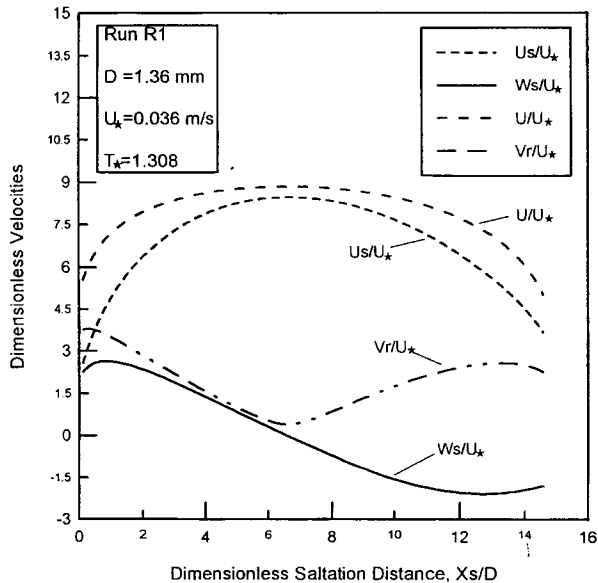


Fig. 14. Simulated saltation velocities under the low transport stage parameter.

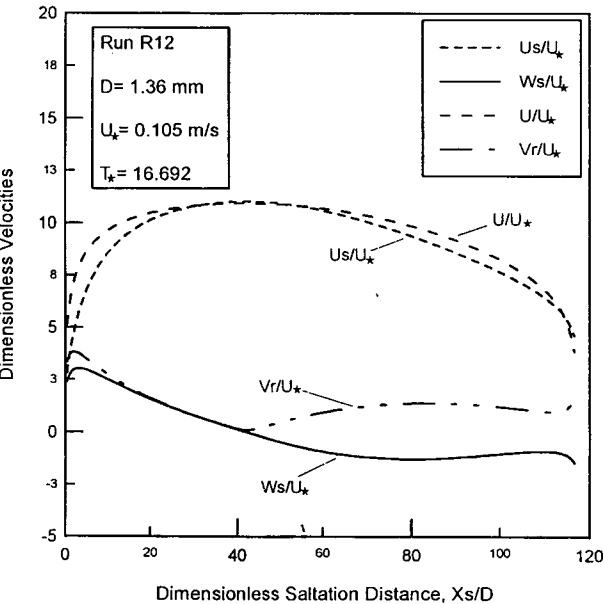


Fig. 15. Simulated saltation velocities under the high transport stage parameter.

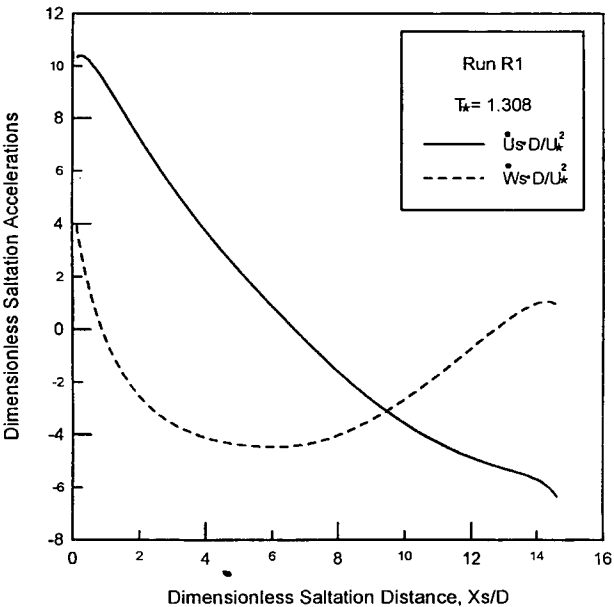


Fig. 16. Simulated particle saltation accelerations.

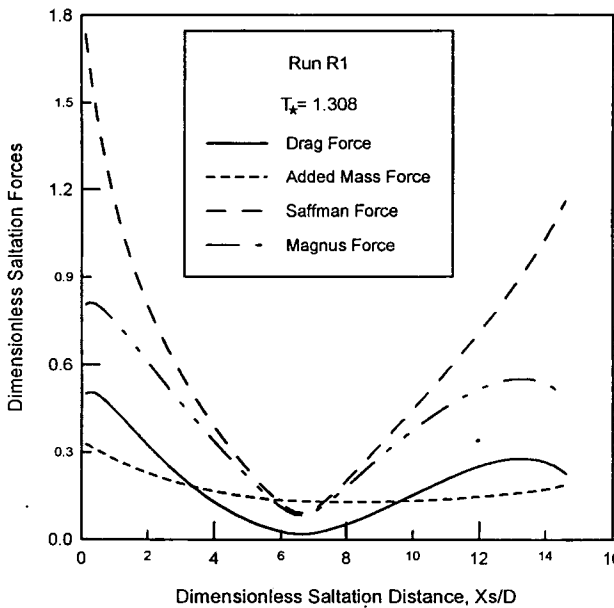


Fig. 17. Longitudinal variations of the acting forces under the saltation process.

in the rising limb, reaches the maximum velocity at the top, and then slows down in the falling limb. The relative velocity is larger for both rising and falling limbs and reaches a minimum value at the top. Under a higher transport stage parameter, the longitudinal component of the saltation velocity is much closer to the flow velocity as T_* increases. The spatial variations of the particle accelerations are shown in the Fig. 16.

The particle accelerates in the rising limb and then decelerates. The spatial variations of the corresponding forces acting along the trajectories were simulated and the results are shown in Fig. 17. The Saffman force and Magnus force are very significant during the process while the variations of the drag forces are not as significant. The Saffman force and Magnus force are significantly larger than the drag force. The added mass force is larger in both the rising and falling limbs.

VII. Conclusions

The hydraulic characteristics of particle saltating motions were investigated experimentally and mathematically in this study, and the important findings are summarized as follows.

The saltation length, height, and average velocity were found to increase as the transport stage parameter increased. The maximum saltation length, height, and average velocity observed in the present study were $106.8 D$, $9.3 D$, and $9.9 U_*$, respectively. Regression equations, i.e., Eqs. (3)-(5), were obtained.

The spinning processes were found to be dominated by top-spin motions under uniform flow conditions. The spinning rate was maximum in the rising limb and then decreased linearly along the saltating trajectory. The average lift-off spinning rates observed in this study were between 11.24 and 31.8 revolutions/sec. The particle spun more rapidly as the sediment transport capacity increased. Regression equations for the dimensionless lift-off spinning rates and longitudinal variations of the spinning rates along the trajectory, i.e., Eqs. (6) and (7), were obtained. These results are also similar to those of Lee and Hsu (1994).

A mathematical model was developed to calculate the saltation trajectory, velocities, and corresponding accelerations. The model was calibrated and verified with the experimental data. It shows that a particle accelerates in the rising limb, reaches a maximum velocity at the top of the trajectory, and then slows down in the falling limb. The Saffman force and Magnus force are significantly larger than the drag force. The added mass force is larger in both the rising and falling limbs. The Magnus effect increases the saltation length and height by up to 20% and, hence, cannot be neglected.

Acknowledgment

This study was supported by the National Science Council of the Republic of China. The writers would like to thank the staff of the Hydraulic Research Laboratory of National Taiwan University for support in conducting the experiments.

Nomenclature

The following symbols are used in this paper:

a	a constant;
C_D	drag coefficient;
$C_{L1,2,3}$	lift coefficient;
D	saltating particle size;
D_r	particle diameter ratio;
D_*	particle parameter;
d	bed particle size;
E_A	added mass force;
E_D	drag force;
E_G	submerged weight;
E_L	lift force;
E_M	Magnus force;
E_S	Saffman force;
$f_{1,2,3}()$	function of ();
g	gravitational acceleration;
H	water depth;
H_S	saltation height;
\bar{H}_S	average saltation height;
K_S	equivalent roughness;
L_S	saltation length;
\bar{L}_S	average saltation length;
m_s	particle mass;
R_S	roughness Reynolds number ($=U_*K_S/\nu$);
R_*	Reynolds number ($=U_*D/\nu$);
S	specific weight;
S_o	bed slope;
T_*	transport stage parameter;
U	longitudinal flow velocity;
U_S	saltation longitudinal velocity;
\bar{U}_S	average longitudinal saltation velocity;
U_S	longitudinal saltation acceleration;
U_*	shear velocity;
U_{*c}	critical shear velocity;
V	flow velocity;
V_S	particle velocity;
V_r	relative particle velocity;
V_{ω}	particle spinning velocity;
W_S	vertical saltation velocity;
\bar{W}_S	average vertical saltation velocity;
W_S	vertical saltation acceleration;
x	longitudinal coordinate;
X_S	saltation distance in x-direction;
Y_S	characteristic of saltation;
\bar{Y}_S	dimensionless characteristic of saltation;
z	vertical coordinate;
z_0	zero velocity level;
Z_S	saltation distance in z-direction;
α_A	area coefficient;
α_M	added mass coefficient;
α_V	volume coefficient;
γ_s	specific weight of sediment;
γ_w	specific weight of fluid;
θ	lift-off angle;
κ	Karman constant;
μ	dynamic viscosity;
ν	kinematic viscosity;
ρ_s	density of sediment;
ρ_w	density of fluid;
ϕ	channel bed slope;

Ω_L	dimensionless lift-off saltation spinning rate;
$\overline{\Omega}_L$	average dimensionless lift-off spinning rate;
ω_L	lift-off saltation spinning rate;
$\overline{\omega}_L$	average lift-off saltation spinning rate;
ω_s	particle spinning rate; and
$\overline{\omega}_s$	average particle spinning rate.

References

- Abbott, J. E. and J. R. D. Francis (1977) Saltation and suspension trajectories of solid grains in a water stream. *Proc., Royal Soc., London, U.K., Ser. A*, **1321**(284), 225-254.
- Chepil, W. S. (1945) Dynamics of wind erosion. I. Nature of movement of soil by wind. *Soil Sci.*, **60**, 305-320.
- Einstein, H. A. (1950) The bed-load function for sediment transportation in open channel flow. *Tech. Bull.*, No. 1026, United States Department of Agriculture, Washington, D.C., U.S.A.
- Fernandez Luque, R. and R. Van Beek (1976) Erosion and transport of bedload sediment. *J. Hydr. Res.*, **14**(2), 127-144.
- Hui, Y. and E. Hu (1991) Saltation characteristics of particle motions in water. *Shuili Xuebao* (in Chinese), **12**, 59-64.
- Lee, H. Y. and I. S. Hsu (1994) Investigation of saltating particle motions. *J. Hydr. Res., ASCE*, **120**(7), 831-845.
- Lee, H. Y. and I. S. Hsu (1996) Particle spinning motion during saltating process. *J. Hydr. Res., ASCE*, **122**(10), 587-590.
- Morsi, S. A. and A. J. Alexander (1972) An investigation of particle trajectories in two-phase flow systems. *J. Fluid Mech.*, **55**(Part 2), 193-208.
- Murphy, P. J. and H. Hooshiari (1982) Saltation in water dynamics. *J. Hydr. Engrg., ASCE*, **108**(11), 1251-1267.
- Rubinow, S. I. and J. B. Keller (1961) The transverse force on a spinning sphere moving in a viscous fluid. *J. Fluid Mech.*, **11**, 447-459.
- Saffman, P. G. (1965) The lift on a small sphere in a slow shear flow. *J. Fluid Mech.*, **31**, 385-400.
- Sekine, M. and H. Kikkawa (1992) Mechanics of saltating grains. *J. Hydr. Engrg., ASCE*, **118**(4), 536-558.
- Van Rijn, L. C. (1984) Sediment transport, part I: bed load transport. *J. Hydr. Engrg., ASCE*, **110**(10), 1431-1456.

近床區域顆粒躍移運動之研究

李鴻源*,** 許盈松**

*國立臺灣大學土木工程學系

**國立臺灣大學水工試驗所

摘 要

水流中近床區域泥砂顆粒躍移機制的研究對於推移載運動理論的發展具有重要的意義。本研究運用「即時一流場顯影技術」與「高速攝影技術」，能在不影響流況的情況下，同時量測許多傳統方法所無法測得之數據，包括泥砂運動軌跡、運動速度及旋轉速度。試驗過程中採用不同顆粒條件和不同水流強度的組合，系統地量測了底床附近顆粒的躍移過程，得出在不同水流強度下躍移顆粒之最大躍高、最大躍長、縱向躍移平均速度及躍移旋轉速度。

本文同時提出顆粒單步躍移歷程之物理模式，在已知水流及顆粒條件下，本模式可模擬顆粒躍移軌跡與躍移過程中之速度、加速度及各作用力之沿程變化特性。與試驗結果相驗證，發現本文所建立的物理模式對近床區域泥砂顆粒躍移特性之模擬相當準確，同時發現躍移過程中的馬格納斯效應為一不可忽略的因素，應該加以考慮。經由本文之研究，可以清楚瞭解躍移顆粒之運動特性，對往後進一步深入探討底床質輸砂量推估之理論研究，有極大的助益。